Engineering Fracture Mechanics 284 (2023) 109261

Contents lists available at ScienceDirect

Engineering Fracture Mechanics

journal homepage: www.elsevier.com/locate/engfracmech

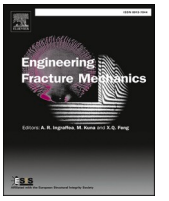

Large deformation and crack propagation analyses of hydrogel by peridynamics

Yujie Chen, Yang Yang *, Yijun Liu *

Department of Mechanics and Aerospace Engineering, Southern University of Science and Technology, Shenzhen, China

ARTICLE INFO

Keywords:
Large deformation
Crack propagation
Peridynamics
Gent model
Hydrogel

ABSTRACT

In this paper, the large tensile deformation and Mode-I crack propagation of hydrogel are effectively simulated by the bond-associated (BA) non-ordinary state-based (NOSB) peridynamics (PD). Based on the nonlocal theory and meshless characteristic, the fracture involving large deformation of hydrogel is solved with simple implementations. In the analysis, the Gent model is first introduced into NOSB PD as the constitutive model to describe the stress-stretch response of hydrogel under a large tensile stretch. The bond-associated scheme is applied to overcome zero-energy modes and numerical oscillation in conventional NOSB PD. Effective stretch criterion is applied to capture the crack propagation. With the explicit dynamic solver, the tensile deformation of a hydrogel sheet with a hole and the crack propagation process of a hydrogel sheet with a pre-notch under pure shear are analyzed. The predicted stress-stretch responses are in good agreement with the experimental observations, which demonstrates the effectiveness and efficiency of the developed PD approach for predicting large deformation and crack propagation of hydrogel.

1. Introduction

Hydrogel is a type of network of one or more polymers suspended in water [1]. As a rubber-like material, hydrogel can possess superb mechanical properties like ultra-high strength, resilience and toughness. The major component water makes hydrogel to possess excellent biocompatibility which can be used in drug delivery and wound dressing [2]. Besides, by introducing ions, hydrogel can also conduct electronic signal to be used for extensile ionotronic devices [3]. With these advantages, hydrogel can be widely used as a smart soft matter in biological medicine, soft robot and other new fields of smart materials and structures [4–6].

The excellent mechanical properties of hydrogel have attracted the attention of researchers in recent years. Many experimental works were carried out to study the large deformation and crack propagation characters of hydrogel [7–9]. However, numerical studies are few, because the constitutive model of hydrogel cannot be properly established due to the complicated material composition. Many models of rubber-type of materials have been proposed. Descriptions of phenomenological rubber elasticity in classical continuum mechanics is based on the assumptions of a homogeneous, isotropic, hyperelastic material for which the strain energy density is expressed as power series in terms of three invariants (I1, I2 and I3) of the right Cauchy-Green strain tensor. Neo-Hookean model [10] is represented by the first term of the series linear in I1. It can capture the stress-stretch response at low stretches in uniaxial tension but fails to predict the response in high stretch regimes. Mooney-Rivlin model [11,12] is constituted by the first and second terms linear in

* Corresponding authors.
E-mail addresses: yangy33@sustech.edu.cn (Y. Yang), liuyj3@sustech.edu.cn (Y. Liu).

https://doi.org/10.1016/j.engfracmech.2023.109261
Received 12 October 2022; Received in revised form 7 March 2023; Accepted 8 April 2023
Available online 15 April 2023

I1 and I2. It can predict the uniaxial tensile behavior for moderate stretches. However, the same parameters show much stiffer response for other states of loading such as biaxial tension. Many other models use the combination of higher order invariants to achieve large-stretch response. Yeoh model [13] involves a third-degree polynomial in I1. Gent model [14] uses a logarithmic function of I1 which in turn can be written in an infinite series containing all degrees of polynomial of I1. These models perform well in predicting the deformation response for moderate to large stretches.

There also exists stretch based and physically based models. Ogden model [15] with many adjustable material parameters that need to be calibrated against experimental data. The difficulty of using these phenomenological models involves an appropriate calibration of the material parameters which bear no physical meaning and their choice requires a caution regarding the satisfaction of Drucker stability postulate. Arruda-Boyce eight chain model [16] and Anand model [17] are physically based models. The advantage of such models is that they usually contain few constitutive parameters and that such parameters are directly connected to the microscopic properties of the material. On the other hand, the main disadvantage is the complexity of such models for analysis and simulation, and the fact that the stress–strain relationship is usually not expressed in an explicit closed form. By comparison, the Gent model not only is based on a simple mathematical framework, but also can be applied over the entire range of strains in hydrogel. Thus, the Gent model has been chosen for the work reported in this paper. In the literature, Li et al. [18] used Gent model for elastic part of the material free energy and captured the deformation and instability in dielectric elastomer composites. Li et al. [19] captured large swelling ratios of polyelectrolyte gels based on Gent model. Wang et al. [20] employed Gent model to analyze large deformation of spherical hydrogel.

Rubber materials show progressive damage and rupture with the increase of loading. This is also the case for hydrogel. Wu et al. employed Arruda–Boyce and model into phase field analysis and captured complex crack patterns [21]. Zhang et al. [22] analyzed dynamic fracture of hyper-elastic materials based on Neo-Hookean models. Peng et al. used Neo-Hookean and Mooney-Rivlin models in smoothed finite element method with phase field model [23], in simulating the Mode I and Mode II cracks. Besides these reported results, simulations of cracks in rubber-like materials are very few in the literature.

Peridynamics (PD) has been developed rapidly to model the initiation and propagation of cracks in various materials and structures, since the first work published in 2000 [24]. PD based on a nonlocal theory, uses integro-differential equations and thereby removes the smoothness requirement of the field variables. Thus, it has inherently advantages in modelling crack initiation and propagation. In PD modeling, the domain is discretized into material points and each point can form a bond to interact with other points within a certain horizon. Failure description means simply removing the interaction between two material points, which makes it convenient to describe complex cracks, especially in 3D cases. The peridynamic differential operators [25] have been demonstrated owing advantages in capturing crack bifurcation [26,27]. Moreover, PD permits multi-scale modeling and can be coupled with molecular dynamics [28], finite element method [29,30], boundary element method [31,32], smooth particle hydrodynamics method [33] and others [34].

Bond-based PD treats the interaction between the two material points as a spring. It can capture the complex crack path and branches in brittle material [35]. However, bond-based PD has a major drawback: the Poisson's ratio is fixed at 1/3 for plane stress cases and 1/4 for plane strain and 3D cases. To solve this problem, state-based PD has been developed. Ordinary state-based PD allows the volume change of a horizon allowing different Poisson's ratio. Xu et al. [36] modeled various hyperplastic models in ordinary state-based PD and presented satisfactory simulation results. Non-ordinary state-based (NOSB) PD builds a bridge to conventional constitutive model by the expression of deformation gradient in PD form [37]. Conventional NOSB PD is known to have zero-energy mode which can cause significant numerical oscillation, due to a non-unique mapping between the deformation states and force states. To overcome zero-energy mode, many modifications have been proposed, such as introducing a fictitious spring force to a bond, using the average displacement over a horizon as a correction [38], and a higher order approximation of deformation gradient [39]. Among the solutions, bond-associated (BA) non-ordinary state-based (NOSB) PD is one of the most promising one, since it uses the points within a bond proximity to calculate its deformation gradient, avoiding the zero-energy mode inherently [40–42]. Based on BA NOSB PD, Behera et al. [43] and Roy et al. [44] analyzed the finite elastic deformation and rupture in Neo-Hookean materials as well as polymers predicted by Anand and Talamini-Mao-Anand (TMA) models, respectively. The numerical results are in good agreement with the experimental data. Ref. [43] and [44] both applied the weak form of peridynamics which is presented by Erdogan et al [45]. Weak form of BA NOSB PD was also demonstrated accuracy with non-uniform discretization [46].

In this paper, the Gent model is applied to predict the response of hydrogel using the BA NOSB PD approach. The material parameters were calibrated through the pure shear test of one type of hydrogel [47]. Effective stretch criterion was applied to predict the crack propagation. Based on an explicit dynamic equation solver, the large deformation of a rectangular hydrogel sheet with a hole under tension is computed. The crack propagation of a pre-notch hydrogel sheet under pure shear is also simulated. The obtained results clearly demonstrate the effectiveness and efficiency of the developed BA NOSB PD approach in simulating the mechanical responses of hydrogel.

2. PD framework

Peridynamics is based on nonlocal interactions. A material point, represented by initial position vector $\mathbf{x}$,can interact with other material points which are within a certain domain (horizon) denoted by $H_{\mathbf{x}}$. Usually, $H_{\mathbf{x}}$ is characterized by a circular (2D) or spherical (3D) region with a radius δ. Any point $\mathbf{x}'$ in $H_{\mathbf{x}}$ is called a neighborhood point of $\mathbf{x}$. The bond vector is defined as $\boldsymbol{\xi} = \mathbf{x}' - \mathbf{x}$. The equation of motion for point $\mathbf{x}$ can be written as:

$$\rho(\mathbf{x})\ddot{\mathbf{u}}(\mathbf{x},t) = \int_{H_{\mathbf{x}}} (\mathbf{t} - \mathbf{t}')\, dV_{\mathbf{x}'} + \mathbf{b}(\mathbf{x},t) \tag{1}$$

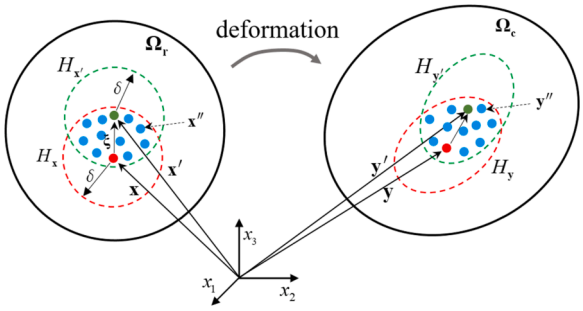

Fig. 1. Bond-associated scheme diagram.

where ρ is the mass density, $\mathbf{u}$ the displacement vector, $\ddot{\mathbf{u}}$ the acceleration vector, $\mathbf{b}$ the body force density vector. $\mathbf{t} = \mathbf{t}(\mathbf{x}, t)$ and $\mathbf{t}' = \mathbf{t}(\mathbf{x}', t)$ are the pair-wise force density vectors, representing the interaction between the material points. The force density vector takes the form of

$$\mathbf{t}(\mathbf{x}, t) = \gamma(s, t) w \mathbf{P}(\mathbf{x}) \mathbf{K}^{-1}(\mathbf{x}) \boldsymbol{\xi} \tag{2}$$

where $\mathbf{P}$ is the first Piola-Kirchhoff stress tensor expressed as

$$\boldsymbol{P}(\mathbf{F}) = \frac{\partial \Psi(\mathbf{F})}{\partial \mathbf{F}} \tag{3}$$

with Ψ being the strain energy density. While, the deformation gradient $\mathbf{F}$ represents a connection between PD with the traditional local theory. The conventional deformation gradient $\mathbf{F}$ in PD expression is point associated and expressed as:

$$\mathbf{F}(\mathbf{x}) = \int_{H_\mathbf{x}} w[(\mathbf{y}' - \mathbf{y}) \otimes (\mathbf{x}' - \mathbf{x})] dV_{\mathbf{x}'} \ \mathbf{K}^{-1}(\mathbf{x}) \tag{4}$$

where $\otimes$ denotes the dyadic product of two vectors, $\mathbf{y}$ is the deformed position vector, w is a scalar valued weight function evaluating the influence of neighborhood points according to their distance $|\boldsymbol{\xi}|$. Different schemes of weight function are listed and analyzed in [48]. In this study, the uniform weight function is used, that is, the value of w is one. $\mathbf{K}$ is the shape tensor defined as

$$\mathbf{K}(\mathbf{x}) = \int_{H_\mathbf{x}} w[(\mathbf{x}' - \mathbf{x}) \otimes (\mathbf{x}' - \mathbf{x})] dV_{\mathbf{x}'} \tag{5}$$

Parameter s is the stretch of a bond defined as

$$s = \frac{|\mathbf{y}' - \mathbf{y}|}{|\mathbf{x}' - \mathbf{x}|} \tag{6}$$

γ is a history-dependent function to include damage description in the material response and can be define as

$$\gamma(s, t) = \begin{cases} 1, & \text{if } s(t') < s_c \text{ for all } 0 \leqslant t' \leqslant t \\ 0, & \text{otherwise} \end{cases} \tag{7}$$

where t is time, s_c is the critical stretch. When the stretch of a bond s exceeds its critical stretch s_c, failure occurs.

3. Bond-associated scheme

Bond-associated scheme is one of the methods to overcome zero-energy modes. As is claimed in [42], the zero-energy modes and the non-unique mapping from deformation states to force states probably root in the point-associated expression of deformation gradient in conventional NOSB PD. As an improvement, bond-associated deformation gradient was proposed, which has been proved effective in accuracy and removing numerical oscillation.

As is shown in Fig. 1, for a bond vector $\boldsymbol{\xi}$ from $\mathbf{x}$ to $\mathbf{x}'$, its bond-associated deformation gradient tensor is computed by considering the intersection region of $H_\mathbf{x}$ and $H_{\mathbf{x}'}$.

The shape tensor in BA NOSB PD is rewritten as

$$\mathbf{K}_\xi(\mathbf{x}) = \int_{H_\mathbf{x} \cap H_{\mathbf{x}'}} w[(\mathbf{x}'' - \mathbf{x}) \otimes (\mathbf{x}'' - \mathbf{x})] dV_{\mathbf{x}''} \tag{8}$$

Its corresponding bond-associated deformation gradient tensor $\mathbf{F}$ is expressed as

$$\mathbf{F}_{\xi}(\mathbf{x}) = \left\{ \int_{H_{\mathbf{x}} \cap H_{\mathbf{x}'}} w[(\mathbf{y}'' - \mathbf{y}) \otimes (\mathbf{x}'' - \mathbf{x})] dV_{\mathbf{x}''} \right\} \mathbf{K}_{\xi}^{-1} \tag{9}$$

The PD strain energy of a bond at material point $\mathbf{x}$ is contributed by all the bonds belonging to the domain of intersections of point $\mathbf{x}$ and $\mathbf{x}''$:

$$\delta W_{\xi}^{PD}(\boldsymbol{x}) = \int_{H_{\mathbf{x}} \cap H_{\mathbf{x}'}} \phi(\mathbf{x}, \mathbf{x}'') \left[(\mathbf{t}''_{\xi} - \mathbf{t}_{\xi})^{T} \delta(\mathbf{y}'' - \mathbf{y}) \right] dV_{\mathbf{x}''} \tag{10}$$

Here, $\phi(\mathbf{x}, \mathbf{x}'')$ is a volume ratio proposed in Ref. [49], allowing non-uniform grid discretization and horizon size, and can be defined as

$$\phi(\mathbf{x}, \mathbf{x}') = \frac{\int_{H_{\mathbf{x}'}} dV_{\mathbf{x}''}}{\int_{H_{\mathbf{x}'}} dV_{\mathbf{x}''} + \int_{H_{\mathbf{x}}} dV_{\mathbf{x}''}} \tag{11}$$

Noted that $\phi(\mathbf{x}, \mathbf{x}') + \phi(\mathbf{x}', \mathbf{x}) = 1$. For a uniform grid discretization and an identical domain of interaction at each material point, $\phi(\mathbf{x}, \mathbf{x}') = \phi(\mathbf{x}', \mathbf{x}) = 1/2$.

In classical continuum mechanics (CM), the variation of strain energy density takes the form of

$$\delta W_{\xi}^{CM}(\mathbf{x}) = tr\left(\mathbf{P}_{\xi}^{\mathrm{T}} \delta \mathbf{F}_{\xi} \right) \tag{12}$$

By substituting of bond-associate deformation gradient tensor of PD, Eq. (12) can be expressed as

$$\delta W_{\xi}^{CM}(\mathbf{x}) = \int_{H_{\mathbf{x}} \cap H_{\mathbf{x}'}} \left[w \mathbf{P}_{\xi} \mathbf{K}_{\xi}^{-1} (\mathbf{x}'' - \mathbf{x}) \right]^{T} \delta(\mathbf{y}'' - \mathbf{y}) dV_{\mathbf{x}''} \tag{13}$$

As is claimed in [41] and [49], there is a relation between Eq. (10) and Eq. (13):

$$\delta W_{\xi}^{PD}(\mathbf{x}) = \phi_{\xi}(\mathbf{x}, \mathbf{x}') \delta W_{\xi}^{CM}(\mathbf{x}) \tag{14}$$

where ϕ_{ξ} is volume fraction defined as

$$\phi_{\xi}(\mathbf{x}, \mathbf{x}') = \frac{\int_{H_{\mathbf{x}} \cap H_{\mathbf{x}'}} dV_{\mathbf{x}''}}{\int_{H_{\mathbf{x}}} dV_{\mathbf{x}''}} \tag{15}$$

Substituting Eqs. (10) and (13) into Eq. (14) leads to

$$\int_{H_{\mathbf{x}} \cap H_{\mathbf{x}'}} \left\{ \phi(\mathbf{x}, \mathbf{x}'') \left[\mathbf{t}_{\xi}(\mathbf{x}) - \mathbf{t}_{\xi}(\mathbf{x}'') \right]^{T} - \phi_{\xi}(\mathbf{x}, \mathbf{x}') \left[w \mathbf{P}_{\xi} \mathbf{K}_{\xi}^{-1} (\mathbf{x}'' - \mathbf{x}) \right]^{T} \right\} \delta(\mathbf{y}'' - \mathbf{y}) dV_{\mathbf{x}''} = 0 \tag{16}$$

Since Eq. (16) is valid for arbitrary variation of $\mathbf{y}'' - \mathbf{y}$, this leads to

$$\mathbf{t}_{\xi}(\mathbf{x}) - \mathbf{t}_{\xi}(\mathbf{x}'') = \frac{\phi_{\xi}(\mathbf{x}, \mathbf{x}')}{\phi(\mathbf{x}, \mathbf{x}'')} w \mathbf{P}_{\xi} \mathbf{K}_{\xi}^{-1} (\mathbf{x}'' - \mathbf{x}) \tag{17}$$

Similarly, consider the strain energy at material point $\mathbf{x}'$ results in

$$\mathbf{t}_{\xi}(\mathbf{x}') - \mathbf{t}_{\xi}(\mathbf{x}'') = \frac{\phi_{\xi}(\mathbf{x}', \mathbf{x})}{\phi(\mathbf{x}', \mathbf{x}'')} w \mathbf{P}'_{\xi} \mathbf{K}'^{-1}_{\xi} (\mathbf{x}'' - \mathbf{x}') \tag{18}$$

Let $\mathbf{x}'' = \mathbf{x}'$ in Eq. (17) and $\mathbf{x}'' = \mathbf{x}$ in Eq. (18) lead to

$$\mathbf{t}_{\xi}(\mathbf{x}) - \mathbf{t}_{\xi}(\mathbf{x}') = \frac{\phi_{\xi}(\mathbf{x}, \mathbf{x}')}{\phi(\mathbf{x}, \mathbf{x}')} w \mathbf{P}_{\xi} \mathbf{K}_{\xi}^{-1} (\mathbf{x}' - \mathbf{x}) \tag{19}$$

and

$$\mathbf{t}_{\xi}(\mathbf{x}') - \mathbf{t}_{\xi}(\mathbf{x}) = \frac{\phi_{\xi}(\mathbf{x}', \mathbf{x})}{\phi(\mathbf{x}', \mathbf{x})} w \mathbf{P}'_{\xi} \mathbf{K}'^{-1}_{\xi} (\mathbf{x} - \mathbf{x}') \tag{20}$$

Combining Eqs. (19) and (20) results in

$$\mathbf{t}_{\xi}(\mathbf{x}) - \mathbf{t}_{\xi}(\mathbf{x}') = \frac{1}{2} \left[\frac{\phi_{\xi}(\mathbf{x}, \mathbf{x}')}{\phi(\mathbf{x}, \mathbf{x}')} w \mathbf{P}_{\xi} \mathbf{K}_{\xi}^{-1} (\mathbf{x}' - \mathbf{x}) - \frac{\phi_{\xi}(\mathbf{x}', \mathbf{x})}{\phi(\mathbf{x}', \mathbf{x})} w \mathbf{P}'_{\xi} \mathbf{K}'^{-1}_{\xi} (\mathbf{x} - \mathbf{x}') \right] \tag{21}$$

which leads to the final expression of force density in bond-associated scheme as:

$$\mathbf{t}_{\xi}(\mathbf{x}) = \frac{1}{2} \frac{\phi_{\xi}(\mathbf{x}, \mathbf{x}')}{\phi(\mathbf{x}, \mathbf{x}')} w \mathbf{P}_{\xi} \mathbf{K}_{\xi}^{-1} (\mathbf{x}' - \mathbf{x}) \tag{22}$$

Along with the history-dependent function γ, expression can be written as:

$$\mathbf{t}_{\xi}(\mathbf{x}) = \frac{1}{2}\gamma(s,t)\frac{\phi_{\xi}(\mathbf{x},\mathbf{x}')}{\phi(\mathbf{x},\mathbf{x}')} w\mathbf{P}_{\xi}\mathbf{K}_{\xi}^{-1}(\mathbf{x}' - \mathbf{x}) \tag{23}$$

4. Constitutive relation for Gent model

Gent model can capture the stress-stretch response of hydrogel under large deformation using an expression, which is the first constitutive model introduced in the BA NOSB PD. In Gent model, the strain energy density can be expressed as:

$$\Psi = -\frac{\mu J_m}{2}\ln\left(1 - \frac{\bar{I}_1 - 3}{J_m}\right) + \frac{1}{D}\left(\frac{J^2 - 1}{2} - \ln J\right) \tag{24}$$

here Ψ is the strain energy density, μ is the shear modulus, J_m represents tensile limit. $\bar{I}_1$ is the normalized first invariant of right Cauchy-Green strain tensor which can be expressed as $\bar{I}_1 = tr\mathbf{C}J^{-2/3}$ with $\mathbf{C} = \mathbf{F}^{\mathrm{T}}\mathbf{F}$ and $J = \det\mathbf{F}$. The second term on the right-hand side is added to represent the effect of volume change. For material with slight compressibility, D can be set to a relatively small value.

By derivative of Ψ with respect to $\mathbf{F}$ gives

$$\frac{\partial\Psi}{\partial\mathbf{F}} = \frac{\mu}{2}\frac{J_m}{J_m - tr\mathbf{C}J^{-2/3} + 3}\left(\frac{\partial tr\mathbf{C}}{\partial\mathbf{F}}J^{-2/3} - \frac{2}{3}tr\mathbf{C}J^{-5/3}\frac{\partial J}{\partial\mathbf{F}}\right) + \frac{1}{D}\left(J\frac{\partial J}{\partial\mathbf{F}} - \frac{1}{J}\frac{\partial J}{\partial\mathbf{F}}\right) \tag{25}$$

and substituting of $\partial tr\mathbf{C}/\partial\mathbf{F} = 2\mathbf{F}$ and $\partial J/\partial\mathbf{F} = J\mathbf{F}^{-T}$ into Eq. (25), the first Piola-Kirchhoff stress tensor $\mathbf{P}$ can be evaluated as

$$\mathbf{P} = \frac{\partial\Psi}{\partial\mathbf{F}} = \frac{\mu J^{-2/3}J_m}{J_m - tr\mathbf{C}J^{-2/3} + 3}\left(\mathbf{F} - \frac{1}{3}tr\mathbf{C}\mathbf{F}^{-T}\right) + \frac{1}{D}(J^2 - 1)\mathbf{F}^{-T} \tag{26}$$

In the following section, we focus on the plane stress case. Under plane stress assumption, conditions can be equivalently imposed on the second Piola-Kirchhoff stress tensor $\mathbf{S}$: $S_{13} = S_{23} = S_{33} = 0$. Then, the second Piola-Kirchhoff stress tensor $\mathbf{S}$ can be obtained according to the first Piola-Kirchhoff stress $\mathbf{P}$ as

$$\mathbf{S} = \mathbf{F}^{-1}\mathbf{P} = \frac{\mu J^{-2/3}J_m}{J_m - tr\mathbf{C}J^{-2/3} + 3}\left(\mathbf{I} - \frac{1}{3}tr\mathbf{C}\mathbf{F}^{-1}\mathbf{F}^{-\mathrm{T}}\right) + \frac{1}{D}(J^2 - 1)\mathbf{F}^{-1}\mathbf{F}^{-\mathrm{T}} \tag{27}$$

Since $\mathbf{C}^{-1} = \mathbf{F}^{-1}\mathbf{F}^{-\mathrm{T}}$,

$$\mathbf{S} = \mathbf{F}^{-1}\mathbf{P} = \frac{\mu J^{-2/3}J_m}{J_m - tr\mathbf{C}J^{-2/3} + 3}\left(\mathbf{I} - \frac{1}{3}tr\mathbf{C}\mathbf{C}^{-1}\right) + \frac{1}{D}(J^2 - 1)\mathbf{C}^{-1} \tag{28}$$

Enforcing $S_{13} = S_{23} = 0$ results in $(C^{-1})_{13} = (C^{-1})_{23} = 0$ and $(C^{-1})_{33} = \frac{1}{C_{33}}$.

Enforcing $S_{33} = 0$ leads to an expression as

$$\frac{\mu J^{-2/3}J_m}{J_m - tr\mathbf{C}J^{-2/3} + 3}\left(C_{33} - \frac{1}{3}tr\mathbf{C}\right) + \frac{1}{D}(J^2 - 1) = 0 \tag{29}$$

Substitute Eq. (29) into Eq. (28) gives

$$\mathbf{S} = \frac{\mu J^{-2/3}J_m}{J_m - tr\mathbf{C}J^{-2/3} + 3}(\mathbf{I} - C_{33}\mathbf{C}^{-1}) \tag{30}$$

Then, the first Piola-Kirchoff stress tensor can be recast into

$$\mathbf{P} = \mathbf{F}\mathbf{S} = \frac{\mu J^{-2/3}J_m}{J_m - tr\mathbf{C}J^{-2/3} + 3}(\mathbf{F} - C_{33}\mathbf{F}^{-\mathrm{T}}) \tag{31}$$

For numerical implementation, $tr\mathbf{C}$ and J are expressed as follows, respectively

$$\begin{aligned} tr\mathbf{C} &= tr\tilde{\mathbf{C}} + C_{33} \\ J &= \sqrt{C_{33}}\tilde{J}, \end{aligned} \tag{32}$$

in which, $tr\mathbf{C} = C_{11} + C_{22}$ and $J = \sqrt{C_{11}C_{22} - C_{12}^2}$. The superscript "~" represents the tensor for 2D case.

Then, C_{33} can be extracted by solving Eqs. (29) which is derived by substituting Eq. (32) into (29)

$$\frac{\mu\tilde{J}^{-2/3}J_m C_{33}^{-1/3}}{J_m - \left(tr\tilde{\mathbf{C}} + C_{33}\right)\tilde{J}^{-2/3}C_{33}^{-1/3} + 3}\left(\frac{2}{3}C_{33} - \frac{1}{3}tr\tilde{\mathbf{C}}\right) + \frac{1}{D}(C_{33}J^2 - 1) = 0 \tag{33}$$

Finally, the first Piola-Kirchhoff stress tensor $\mathbf{P}$ can be obtained as

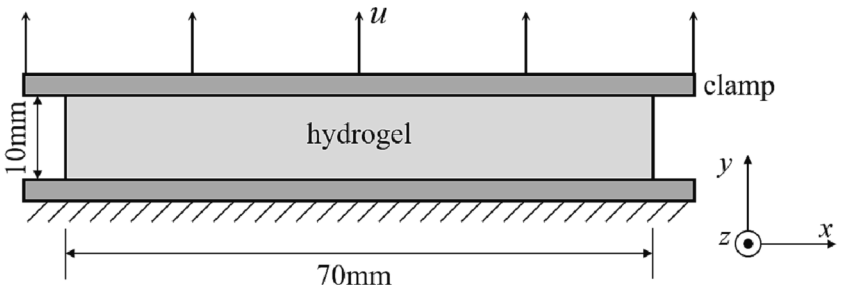

Fig. 2. Illustration of pure shear test.

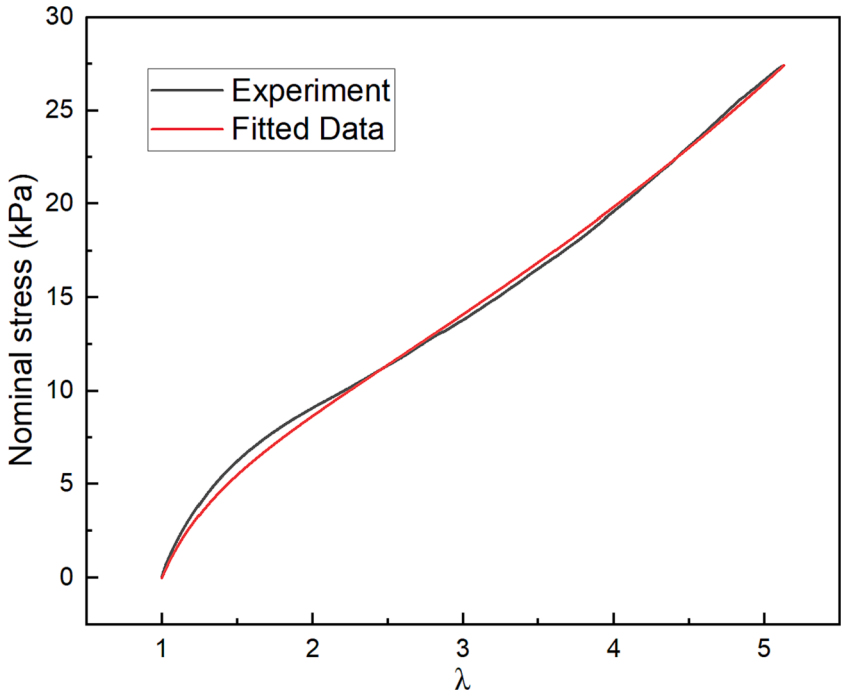

Fig. 3. Stress-stretch response of pure shear test given by experiment and fitted data.

$$\mathbf{P}=\frac{\mu\tilde{J}^{-2/3}J_m C_{33}^{-1/3}}{J_m-\left(tr\tilde{\mathbf{C}}+C_{33}\right)\tilde{J}^{-2/3}C_{33}^{-1/3}+3}\left(\tilde{\mathbf{F}}-C_{33}\tilde{\mathbf{F}}^{-\mathrm{T}}\right) \tag{34}$$

5. Determination of material parameters

Pure shear test is one of the commonly used methods to characterize the material parameters of hydrogel. As shown in Fig. 2, the top and bottom ends of a rectangular sheet hydrogel was clamped. The effective dimension is 10 mm by 70 mm and the thickness is 3 mm. It was elongated slowly in the y direction. The top clamp was connected to a force tensor to output the displacements and its corresponding nominal stresses. The detailed experiment conditions are described in [47].

Parameters λ_x, λ_y and λ_z are defined to be the ratio of the current length to the initial length of the hydrogel along x, y and z direction respectively. Due to the assumption of incompressibility, it is assumed $\lambda_x=1$, $\lambda_y=\lambda$ and $\lambda_z=1/\lambda$. In this specific loading condition, the strain energy density can be written as

$$\Psi=-\frac{\mu J_m}{2}\ln\left(1-\frac{\lambda_x^2+\lambda_y^2+\lambda_z^2-3}{J_m}\right)=-\frac{\mu J_m}{2}\ln\left(\frac{J_m-\lambda^2-\lambda^{-2}-2}{J_m}\right) \tag{35}$$

Nominal stress measured by the sensor can be expressed as

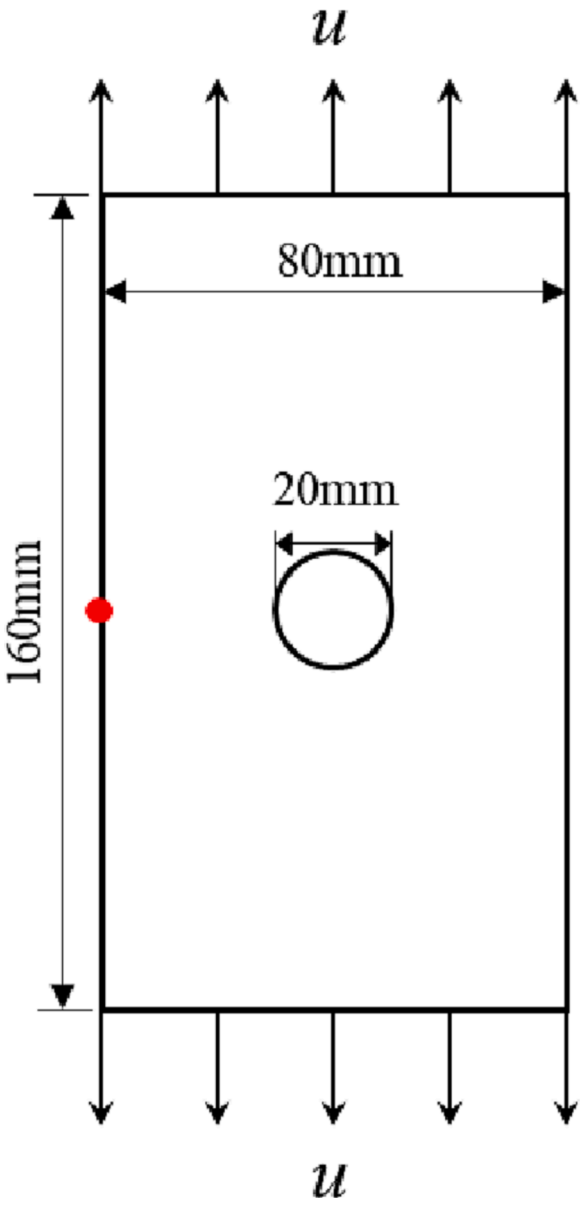

Fig. 4. A rectangular hydrogel sheet with a hole in the center.

$$s = \frac{\partial \Psi}{\partial \lambda_y} = \frac{\mu J_m (\lambda - \lambda^{-3})}{J_m - \lambda^2 - \lambda^{-2} + 2} \tag{36}$$

The values of μ and J_m can be evaluated by fitting the Eq. (36) to the experimental data. Fig. 3 shows the experimental data and the fitted line with the least square method. The resulted μ and J_m are 4.55 kPa and 162.6, respectively.

6. Numerical results

In the following sections, three numerical examples using the developed PD approach are presented. For convenience, in all cases λ represents the stretch ratio along the loading direction unless otherwise specified.

6.1. Tension test of a hydrogel sheet with a hole

A rectangular hydrogel sheet with a center hole having a diameter of 20 mm is studied. The width and length of the sheet are 80 mm and 160 mm, respectively, as shown in Fig. 4. Symmetric tensile displacement is applied on the top and bottom edges. The left and right

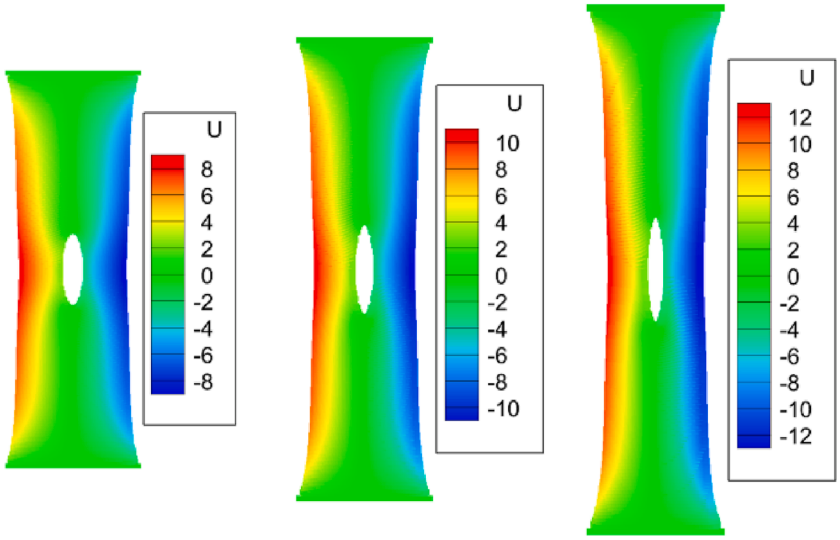

Fig. 5. Contour plots of horizontal displacement under $\lambda = 1.5$, 1.75 and 2.0. The unit of the contour is millimeter.

Table 1
The comparison of maximum horizontal displacements between present results and FEM.

λ	U_{max_FEA}(mm)	$\delta = 2.515$dx		$\delta = 3.015$dx		$\delta = 3.515$dx	
		U_{max_PD} (mm)	*error (%)*	U_{max_PD} (mm)	*error (%)*	U_{max_PD}(mm)	*error(%)*
1.50	**8.62**	**8.48**	**1.62**	**8.43**	**2.20**	**8.40**	**2.60**
1.75	**11.10**	**10.94**	**1.44**	**10.87**	**2.07**	**10.85**	**2.25**
2.00	**13.01**	**12.81**	**1.54**	**12.75**	**2.00**	**12.73**	**2.15**

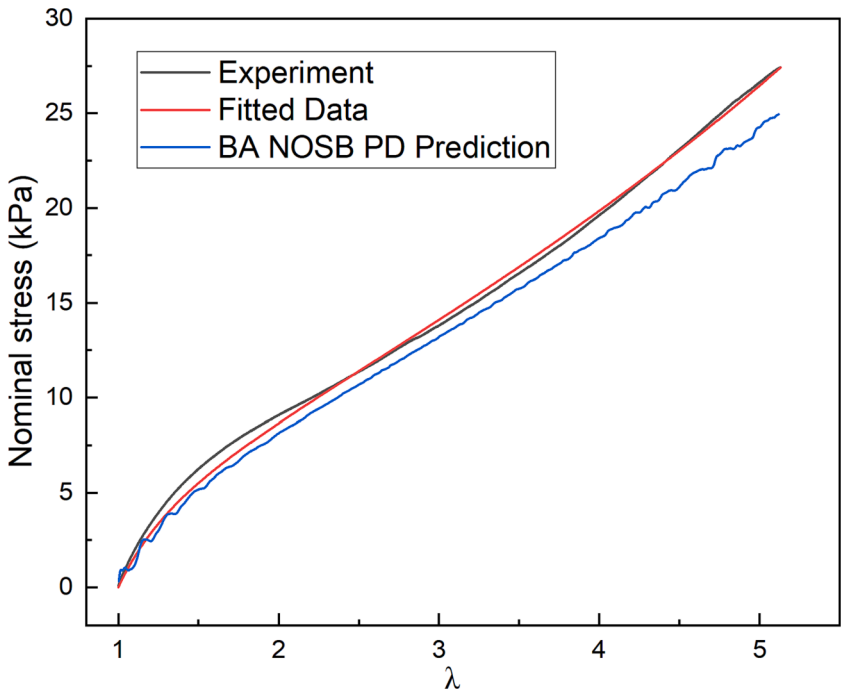

Fig. 6. The comparison of nominal stresses of pure shear test between experiment, fitted data and BA NOSB PD prediction.

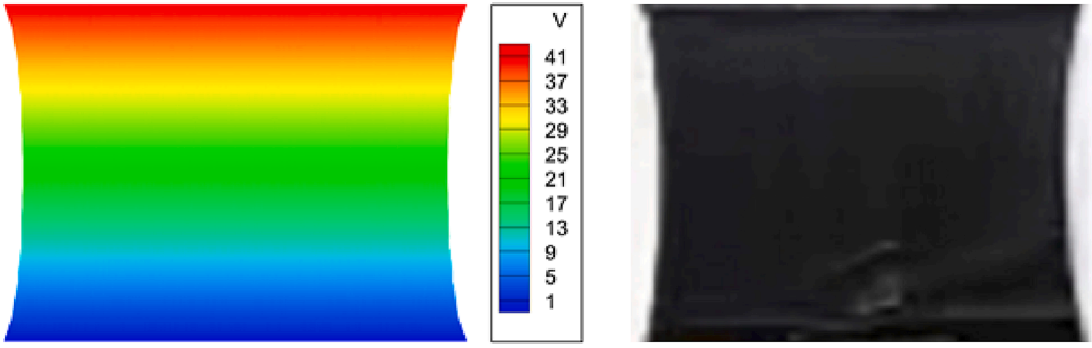

Fig. 7. Vertical displacement contour (left) and experiment photo (right) at $\lambda = 5.125$. The unit of the contour is millimeter.

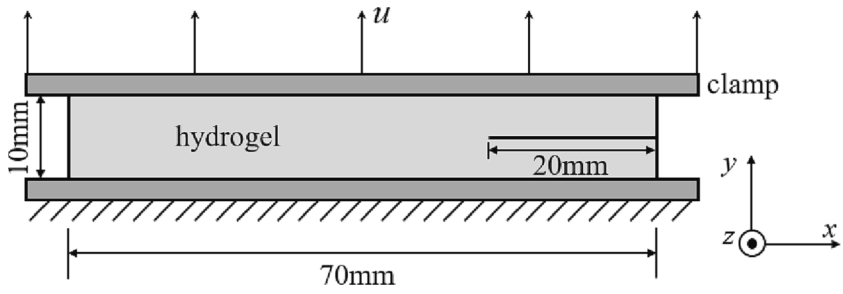

Fig. 8. Pure shear of a hydrogel sheet with a pre-notch.

edges are free of loading. The sample is treated as plane stress case. In PD modeling, the domain is discretized into 80x160 material points uniformly which leads to the spatial discretization size dx of 1 mm and the points within the hole are removed. The displacements applied on the top and bottom layer of points increased gradually and then maintained at a fixed value to obtain a static solution. Simulations were performed with the horizon size $\delta = 2.515dx$, $3.015dx$ and $3.515dx$.

Fig. 5 shows the horizontal displacement under $3.015dx$ at $\lambda = 1.5$, 1.75 and 2.0. The maximum horizontal displacement $u_{\max}$ locates at the midpoint on the left edge, i.e., the red point in Fig. 4. FEA was also performed with the same material parameters and loading conditions using ANSYS with 2014 quadratic quadrilateral elements. The relative difference is defined as

$$error = \left| \frac{u_{\max\_FEA} - u_{\max\_PD}}{u_{\max\_FEA}} \right| \times 100\% \tag{37}$$

Table 1 shows the comparison of stretch ratio between present method and FEM. The differences of stretch ratio for different horizon size are all within 3% which implies the very good agreement of present method with FEA predictions.

For δ smaller than $2.515dx$, there are bit mutual material points for a bond, resulting in less accuracy in evaluating deformation gradient. For δ larger $3.515dx$, too many neighborhood points would result in significant computational cost. It can also be observed that the error increased as δ increased. One of the reasons is surface effect [50]: the stiffness of points on the edge or at the corner varies since they do not have enough neighborhood as the point in the bulk. Moreover, Daniele et al. [51] pointed out that for failure prediction, δ should be lager enough to overcome the dependency of crack path on the orientation of grids, and suggested δ should be larger than $3dx$ [51]. Thus, δ is set to $3.015dx$ in the following samples.

6.2. Validation using a hydrogel sheet

The hydrogel sheet model shown in Fig. 2 is studied in this section. The bottom edge is fixed. The top edge was applied with a small velocity, moving upward gradually, until $\lambda = 5.125$. The nominal stress was calculated during the loading process, as shown in Fig. 6. The predicted stress is less than the experiment data, with the error within 10% in general. Except surface effect, the primary cause of the error is from the determination of material parameters: λ_x is assumed to be 1.0. While horizontal shrink would certainly occur, leading to less nominal stress detected. To overcome this deviation originated form data fitting, the fitted value can be set a little larger than experiment data deliberately. The vertical displacement under $\lambda = 5.125$ is shown in Fig. 7. The corresponding deformation profile is in good agreement with the experimental data shown in Fig. 7.

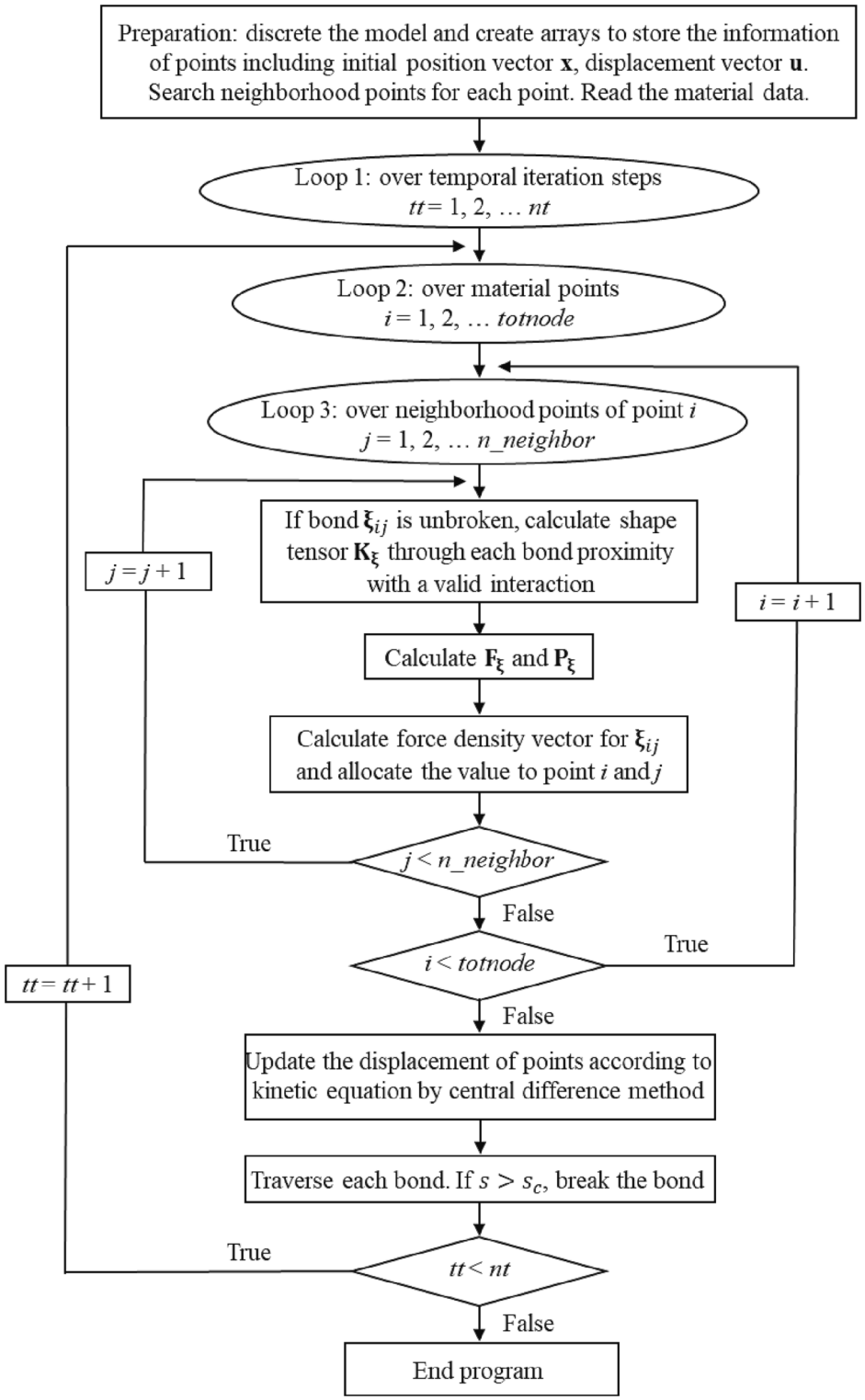

Fig. 9. Flowchart of the failure prediction.

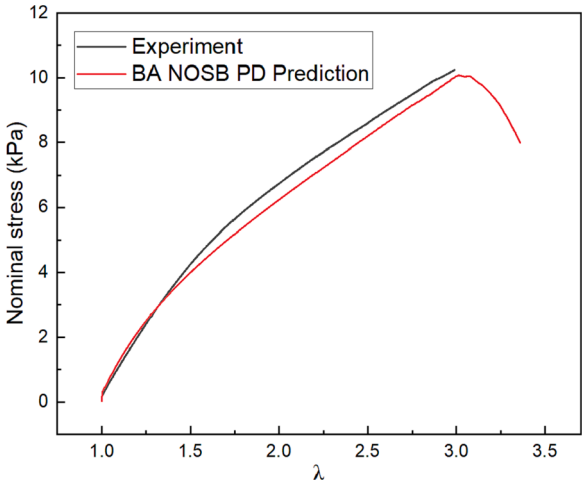

Fig. 10. The comparison of nominal stresses of a hydrogel sheet with a pre-notch between experiment and BA NOSB PD prediction.

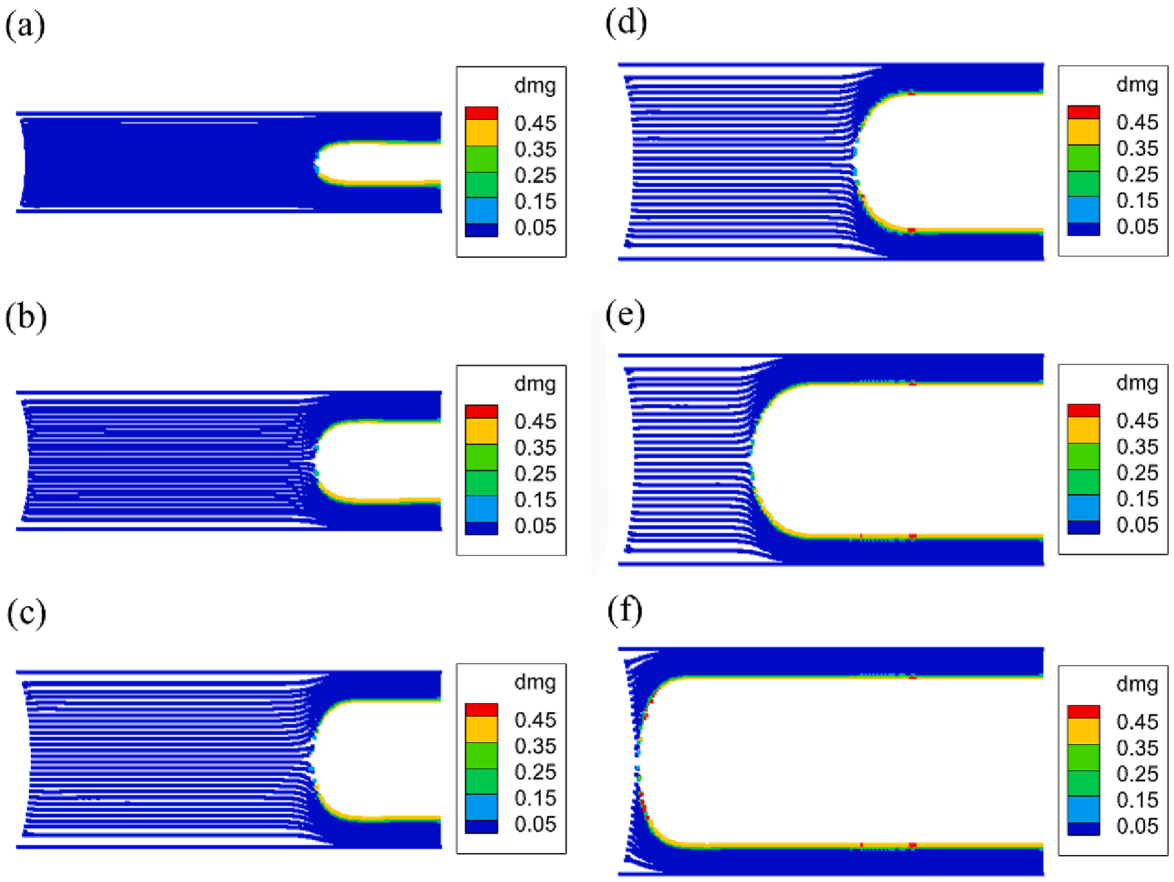

Fig. 11. PD prediction of the deformation and crack propagation of hydrogel sample.

6.3. Crack propagation analysis of a hydrogel sheet with a pre-notch under pure shear

A 20-millimeter pre-notch was introduced on the middle of right edge, as shown in Fig. 8. The domain is divided into 210x30 material points. The bottom edge is fixed. Displacement is applied on the top edge. For pre-notch modelling, bonds passing through pre-notch are removed.

There exist various criteria for bond breakage. Many criteria are based on fracture energy. An in-depth study of the relation between critical stretch and energy release rate was performed by Yu and Li [52]. Stress tensor-based criteria can also govern the crack propagation [53]. Crack tip of hyperplastic material can be regarded as a circular arc in Mode-I crack and material near the crack tip is under uniaxial tension [54]. Therefore, the failure at the crack tip of hyperplastic material is assumed to occurred when bond stretch s exceeds s_c, which is the effective stretch criterion for hyperplastic material. The value of s_c should be calibrated through the simulation or the experiments [43]. According to the calibration and experimental data, the maximum bond stretch is around 7.2 when failure occurred. Thus s_c is set to 7.2 in this simulation. The flowchart of the present method is presented in Fig. 9.

The nominal stress predicted by using BA NOSB PD and experiment data are plotted in Fig. 10. The progressive damages of the hydrogel sheet are plotted in Fig. 11, where the damage of a material point $dmg(\mathbf{x})$ is defined as

$$dmg(\mathbf{x}) = 1 - \frac{\int_{H_\mathbf{x}} \gamma\left(s_{(\boldsymbol{\xi})}, t\right) dV_{\mathbf{x}'}}{\int_{H_\mathbf{x}} dV_{\mathbf{x}'}} \tag{38}$$

When the loading stretch ratio is larger than 3, the number of bond breakage surged indicating the progressive failure propagation. In this state, the propagated crack released much elastic energy and the released energy accelerated crack propagation. The nominal stress before progressive failure is 10.05 kPa from BA NOSB PD prediction and 10.25 kPa from experiment. The error is 2%. The source of the error is similar as discussed in the previous part. The results illustrate the present model can be applied to analyze the stable crack propagation and is valid to predict the start of the progressive crack propagation of hydrogel.

7. Conclusions

In this paper, a BA NOSB PD approach is presented to predict the large deformation and Mode I crack propagation of hydrogel. The Gent model is employed for the constitutive relation under large stretch of the hydrogel. The kinetic equation is based on bond-associated deformation gradient to avoid zero-energy modes. Verification and validation of the approach and model are performed through comparisons of the present results with those of the FEA prediction, as well as the data from experiments in the absence of failure. Adopting the effective stretch as the failure criterion, crack propagation analysis of hydrogel sheets with a pre-notch is simulated. The numerical results show a very good agreement with the experimental results. The developed BA NOSB PD approach and model are found to be effective and efficient in modeling the large deformation and fracture of hydrogel.

CRediT authorship contribution statement

Yujie Chen: Data curation, Writing - original draft, Visualization, Investigation, Validation, Formal analysis, Software.**Yang Yang:** Project administration, Methodology, Funding acquisition, Conceptualization, Supervision, Writing - original draft, Writing - review & editing. **Yijun Liu:** Conceptualization.

Declaration of Competing Interest

The authors declare that they have no known competing financial interests or personal relationships that could have appeared to influence the work reported in this paper.

Data availability

No data was used for the research described in the article.

Acknowledgements

The authors would like to thank the financial support from the National Natural Science Foundation of China (Project Nos. 12272160), the Natural Science Foundation of Guangdong Province (No. 2020A1515010685), and the Department of Education of Guangdong Province (No. 2020ZDZX2008). We would also like to thank Professor Canhui Yang for providing the data of hydrogel experiments.

References

[1] Enas M, Ahmed. Hydrogel: preparation, characterization, and applications: a review. J Adv Res 2015;6:105–21.
[2] Peppas NA, Hilt JZ, Khademhosseini A, Langer R. Hydrogels in biology and medicine: from molecular principles to bionanotechnology. Adv Mater 2006;18:1345–60.
[3] Yang CH, Suo ZG. Hydrogel ionotronics. Nat Rev Mater 2018;3(6):125–42.
[4] Lee YW, Chun S, Son D, Hu XH, Schneider M, Sitti M. A tissue adhesion-controllable and biocompatible small-scale hydrogel adhesive robot. Adv Mater 2022;34(13):2109325.
[5] Hamidi M, Azadi A, Rafiei P. Hydrogel nanoparticles in drug delivery. Adv Drug Deliv Rev 2008;60(15):1638–49.
[6] Sun JY, Zhao XH, Illeperuma WRK, Chaudhuri O, Oh KH, Mooney DJ, et al. Highly stretchable and tough hydrogels. Nature 2012;489(7414):133–6.
[7] Zhang Y, Fukao K, Matsuda T, Nakajima T. Unique crack propagation of double network hydrogels under high stretch. Extreme Mech Lett 2021;51:101588.
[8] He YF, Wan XD, Chen YJ, Yang CH. Enhance the debonding resistance of hydrogel by large-scale bridging. J Mech Phys Solids 2021;155:104570.
[9] Liu MC, Guo JY, Hui CY, Zehbder A. Crack tip stress based kinetic fracture model of a PVA dual-crosslink hydrogel. Extreme Mech. Lett. 2019;29:100457.

[10] Treloar LRG. The elasticity of a network of long-chain molecules – II. Trans Faraday Soc 1943;39:241–6.
[11] Mooney M. A theory of large elastic deformation. J Appl Phys 1940;11:582–92.
[12] Rivlin RS. Large elastic deformations of isotropic materials: I, fundamental concepts. II. Some uniqueness theorem for pure homogeneous deformation. Phil Trans R Soc A 1948;240:459–508.
[13] Yeoh OH. Some forms of the strain energy function for rubber. Rubber Chem Technol 1993;66(5):754–71.
[14] Gent AN. A new constitutive relation for rubber. Rubber Chem Technol 1996;69:59–61.
[15] Ogden RW. Large deformation isotropic elasticity–on the correlation of theory and experiment for incompressible rubberlike solids, Proc. R. Soc. A 1972;326: 565–84.
[16] Arruda EM, Boyce MC. A three-dimensional constitutive model for the large stretch behavior of rubber elastic materials. J Mech Phys Solids 1993;41:389–412.
[17] Anand L. A constitutive model for compressible elastomeric solids. Comput Mech 1996;18:339–55.
[18] Li WY, Landis CM. Deformation and instabilities in dielectric elastomer composites. Smart Mater Struct 2012;21:094006.
[19] Li JY, Suo ZG, Vlassak JJ. A model of ideal elastomeric gels for polyelectrolyte gels. Soft Matter 2014;10:2582.
[20] Wang HM, Yang JP. Quantifying the equilibrium swelling responses and swelling-induced snap-through of heterogeneous spherical hydrogels. J Intell Mater Syst Struct 2021;32:113–23.
[21] Wu J, Mcauliffe C, Waisman H, Deodatis G. Stochastic analysis of polymer composites rupture at large deformations modeled by a phase field method. Comput Methods Appl Mech Engng 2016;312:596–634.
[22] Zhang ZJ, Qiu YS, Hu ZQ, Ye HF, Zhang HW, Zheng YG. Explicit phase-field total Lagrangian material point method for the dynamic fracture of hyperelastic materials. Comput Methods Appl Mech Engng 2022;398:115234.
[23] Peng F, Huang W, Zhang ZQ, Guo TF, Ma YE. Phase field simulation for fracture behavior of hyperelastic material at large deformation based on edge-based smoothed finite element method. Engng Fract Mech 2020;238:107233.
[24] Silling SA. Reformulation of elasticity theory for discontinuities and long-range forces. J Mech Phys Solids 2000;48:175–209.
[25] Bergel GL, Li S. The total and updated Lagrangian formulation of state-based peridynamics. Comput Mech 2016;58:351–70.
[26] Madenci E, Barut A, Dorduncu M. Peridynamic differential operator for numerical analysis. New York: Springer; 2019.
[27] Kan X, Yn J, Li S, Zhang AM. On differences and comparisons of peridynamic differential operators and nonlocal differential operators. Comput Mech 2021;68: 1349–13677.
[28] Tong Q, Li SF. A concurrent multiscale study of dynamic fracture. Comput Methods Appl Mech Engng 2020;366:113075.
[29] Zaccariotto M, Mudric T, Tomasi D, Shojaei A, Galvanetto U. Coupling of FEM meshes with Peridynamic grids. Comput Methods Appl Mech Engng 2018;330: 471–97.
[30] Madenci E, Dorduncu M, Barut A, Phan N. A state-based peridynamic analysis in a finite element framework 2018;195:104-128.
[31] Yang Y, Liu YJ. Modeling of cracks in two-dimensional elastic bodies by coupling the boundary element method with peridynamics. Int J Solids Struct 2021; 217–218:74–89.
[32] Yang Y, Liu YJ. Analysis of dynamic crack propagation in two-dimensional elastic bodies by coupling the boundary element method and the bond-based peridynamics. Comput Methods Appl Mech Engng 2022;399:115339.
[33] Fan H, Li S. A Peridynamics-SPH modeling and simulation of blast fragmentation of soil under buried explosive loads. Comput Methods Appl Mech Engng 2017; 318:349–81.
[34] Lai X, Liu L, Wang Z. A Non-ordinary state-based peridynamics modeling of fractures in quasi-brittle materials. Int J Impact Eng 2018;111:130–46.
[35] Ha YD, Bobaru F. Characteristics of dynamic brittle fracture captured with peridynamics. Engng Fract Mech 2011;78:1156–68.
[36] Xu LY, He XW, Chen W, Li S, Wang GP. Reformulating hyperelastic materials with peridynamic modeling. Pacific Graphics 2018;37:13553.
[37] Silling SA, Epton M, Weckner O, Xu JF, Askari E. Peridynamic states and constitutive modeling. J Elast 2007;88:151–84.
[38] Breitenfeld MS, Geubelle PH, Weckner O, Silling SA. Non-ordinary state-based peridynamic analysis of stationary crack problems. Comput Methods Appl Mech Engng 2014;272:233–50.
[39] Yaghoobi A, Chorzepa MG. Higher-order approximation to suppress the zero-energy mode in non-ordinary state-based peridynamics. Comput Struct 2017;188: 63–79.
[40] Chen HL, Spencer BW. Peridynamic bond-associated correspondence model: stability and convergence properties. Int J Numer Meth Engng 2018;117(6): 713–27.
[41] Chen HL. Bond-associated deformation gradients for peridynamic correspondence model. Mech Res Commun 2018;90:34–41.
[42] Gu X, Zhang Q, Madenci E, Xia X. Possible causes of numerical oscillations in non-ordinary state-based peridynamics and a bond-associated higher-order stabilized model. Comp Methods Appl Mech Eng 2019;357:112592.1-112592.36.
[43] Behera D, Roy P, Madenci E. Peridynamic correspondence model for finite elastic deformation and rupture in Neo-Hookean materials. Int J Non Linear Mech 2020;126:103564.
[44] Roy P, Behera D, Madenci E. Peridynamic simulation of finite elastic deformation and rupture in polymers. Engng Fract Mech 2020;236:107226.
[45] Madenci E, Dorduncu M, Barut A, Phan N. Weak form of peridynamics for nonlocal essential and naural boundary conditions. Comput Methods Appl Mech Engng 2018;337:598–631.
[46] Madenci E, Dorduncu M, Phan N, Gu X. Weak form of bond-associated non-ordinary state-based peridynamics free of zero energy modes with uniform or non-uniform discretization. Engng Fract Mech 2019;218:106613.
[47] Zhang P, Xu ZY, Wu ZY, Xu P, Yang CH. Strengthening poly(2-hydroxyethyl methacrylate) hydrogels using biochars and hydrophobic aggregations. Int J Smart Nano Mater 2022.
[48] Li S, Jin YL, Lu HN, Sun PF, Huang XH, Chen ZY. Wave dispersion and quantitative accuracy analysis of bond-based peridynamic models with different attenuation functions. Comput Mater Sci 2021;197:110667.
[49] Hu Y, Chen HL, Spencer BW, Madenci E. Thermomechanical peridynamic analysis with irregular non-uniform domain discretization. Engng Fract Mech 2018; 197:92–113.
[50] Lel QV, Bobaru F. Surface corrections for peridynamic models in elasticity and fracture. Comput Mech 2018;61:499–518.
[51] Dipasquale D, Sarego G, Zaccariotto M, Galvanetto U. Dependence of crack paths on the orientation of regular 2D peridynamic grids. Engng Fract Mech 2016; 160:248–63.
[52] Yu H, Li S. On energy release rates in Peridynamics. J Mech Phys Solids 2020;142:104024.
[53] Dipasquale D, Sarego G, Prapamonthon P, Yooyen S, Shojaei A. A stress tensor-based failure criterion for ordinary state-based peridynamic models. J Appl Comput Mech 2022;8(2):617–28.
[54] Ayatollahi MR, Mahdi HM, Dehghany M, Berto F. A new criterion for rupture assessment of rubber-like materials under mode-I crack loading: the effective stretch criterion. Adv Engng Mater 2016;18(8):1364–70.